MAGNETIC PROPERTIES OF HITPERM ($Fe_xCo)_{85}Zr_7B_4Cu_1$ NANOCRYSTALLINE MAGNETS (INVITED)

M. A. WILLARD*, M. GINGRAS*, M. J. LEE*, V. G. HARRIS**, D. E. LAUGHLIN*, AND M. E. McHENRY*

* Materials Science and Engineering, Carnegie Mellon University, Pittsburgh, PA 15213-3890
** Naval Research Laboratory, Washington, D.C., 20375-5000

ABSTRACT

Alloys consisting of Fe-Co-M-B-Cu (with M = Zr, Hf, Nb), called HITPERM alloys, have been developed. Synchrotron X-radiation studies have been used to show that the ferromagnetic phase in an equiatomic FeCo-based alloy is the α'-FeCo phase. Since both the α'-FeCo phase and the FeCo-based amorphous phase of the nanocrystalline alloy have high Curie temperatures, a high magnetization persists up to the α -> γ structural phase transformation temperature of 980°C. Room temperature AC permeability measurements have shown that the alloys maintain a high permeability of ~2000 up to a frequency of 20 kHz. The room temperature core loss has also been shown to be competitive with commercial high temperature magnetic alloys with a value of 1 W/g at B_s = 10 kG and f = 10 kHz. Analysis of extended X-ray absorption fine structure (EXAFS) data is consistent with a two-phase mixture of nanocrystalline body centered cubic derivative FeCo structure and an amorphous Zr-rich phase. A differential scanning calorimetry study of the primary crystallization reaction shows an activation energy of 323.3 kJ/mol. As a preliminary study of phase and grain stability, broadening of X-ray diffraction peaks indicates little grain growth after annealing at 600 °C for 3072 hours.

INTRODUCTION

During the past decade, magnetic materials have been developed that demonstrate the favorable role that a nanocrystalline microstructure can have on extrinsic soft magnetic properties. The first of these alloys was based on the nanocrystallization of α-Fe_3Si from an amorphous precursor alloys with components Fe-Nb-Si-B-Cu (FINEMET)[1]. The next class of nanocrystalline alloys, relying on α-Fe nanocrystals, was developed by Suzuki et al. from an alloy of the composition Fe-Zr-B-Cu (NANOPERM)[2-3]. Most recently, magnets based on the α'-FeCo phase have been developed from alloys with composition Fe-Co-Zr-B-Cu.[5] These materials have been found to consist of a two-phase microstructure with a crystalline phase and an amorphous grain boundary phase. As seen in Table I, each alloy has its own distinct properties which makes it good for a certain set of soft magnetic applications.

Sample	Nanocrystal Phase	T_{x1} (K)	T_{x2} (K)	B_s (T)	μ_e	H_c (A/m)
FINEMET $Fe_{73.5}Si_{13.5}B_6Nb_3Cu_1$	α -FeSi	770-815	905-965	1.21 - 1.24	7 – 100k	0.5 – 1.4
NANOPERM $Fe_{88}B_4Zr_7Cu_1$	α -Fe	750-800	990-1000	1.52 – 1.64	3.5 – 48k	2.4 – 4.5
HITPERM $Fe_{44}Co_{44}B_4Zr_7Cu_1$	α' -FeCo	720-750	990-1000	1.6 - 2.0	1 - 2.5k	80-200

Table I: Comparison of various properties for three different classes of nanocrystalline soft magnetic materials.[4]

The focus of this paper is to describe the structure and magnetic properties of the latter alloy (HITPERM)[5-7]. One of the proposed applications for HITPERM is high temperature power generation in jet aircraft. For these applications the demands on bulk soft magnetic materials include (1) higher combined induction and permeability, (2) magnets capable of operating at higher

Mat. Res. Soc. Symp. Proc. Vol. 577 © 1999 Materials Research Society

temperatures, and (3) many non-magnetic issues such as mechanical properties, corrosion resistance, etc. The niche for these materials has been found due to their compromise between the good high frequency response of the residual amorphous phase and the high magnetization of the nanocrystalline phase. As discussed below, HITPERM combines the high permeability of nanocrystalline alloys of this genre with the attractive high induction and Curie temperature associated with FeCo alloys in general.

EXPERIMENT

Ingots with composition $Fe_{44}Co_{44}Zr_7B_4Cu_1$ were arc melted in an argon atmosphere starting with high purity Fe, Co, Zr, Fe_2B, and Cu components. Amorphous ribbons were then produced from the ingots using a standard single wheel melt spinning technique. The amorphous ribbons obtained by this process were about 1 mm in width and 20-50 μm in thickness. After obtaining the as-spun ribbons from the melt spinning procedure, they were isothermally annealed (510 °C < T_{ann} < 700 °C) in an argon atmosphere for 1 hour followed by water quenching. The annealing process resulted in a nanocrystalline microstructure.

Differential thermal analysis (DTA) was used to examine the crystallization temperatures of the as-cast ribbon. A scan rate of 10 °C/min was used between temperatures of 400 and 1200 °C. Synchrotron X-ray diffraction experiments were performed at the National Synchrotron Light Source. These were used to identify superlattice reflections which are signatures of the ordered α'-FeCo phase (B2). X-rays with energy of 7112 eV (or equivalently a wavelength of 1.748 Å) were used for the synchrotron X-ray experiments. This wavelength was chosen to take advantage of the anomalous scattering just above the Fe K-edge.

Kinetics studies were carried out using a Perkin Elmer DSC-7 differential scanning calorimeter (DSC). Temperature scan rates were varied between 5 and 40 °C/min over the temperature range 100 °C to 580 °C. Standard Kissinger analysis was used to find the activation energy of primary crystallization in the amorphous HITPERM alloy.

Long term annealing experiments were conducted at 600 °C for 10, 31, 100, 308, 1000, and 3072 hours. The crystal structure and grain sizes of these samples were examined by X-ray diffraction (XRD) using a Rigaku Θ/ Θ diffractometer, and Cu K_α radiation. The grain sizes were estimated by standard Scherrer analysis with background removal by linear fit.

Extended X-ray absorption fine structure (EXAFS) measurements were used to examine the two-phase microstructure of the HITPERM alloy. X-ray absorption spectra of the Fe, Co, Zr, and Cu K edges were collected from amorphous and nanocrystalline ribbons on Beamlines X23B (NRL) and X23A2 (NIST) at the National Synchrotron Light Source (Brookhaven National Laboratory). Data collection was performed on ribbon samples in transmission and fluorescence yield modes simultaneously. Artifacts were identified by comparison of the two data sets and multiple scans of each sample were performed for improved statistics.[8]

A Vibrating Sample Magnetometer (VSM) was used to measure the magnetization as a function of temperature of the as-quenched alloy from room temperature to 1000 °C, in a field of 500 Oe, and with a heating rate of 2 °C/min. A Walker AC permeameter was used to measure the room temperature permeability and coercivity of toroidal samples. The as-spun ribbons were prepared for permeability measurement by winding them into laminated toroids followed by the standard isothermal anneal for nanocrystallization prior to measurement of AC properties.

RESULTS

A. Microstructure Development

DTA data were collected to identify the region where a single ferromagnetic phase would be crystallized from the amorphous precursor. As seen in Figure 1, the primary crystallization peak (T_{x1}), corresponding to the crystallization of α'-FeCo, was found at 500 °C. Other crystalline phases began to form at temperatures above 700 °C, which allowed for a 200 °C range where nanocrystallization of only the desired ferromagnetic α'-FeCo formed.

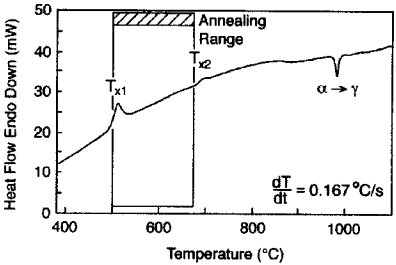

Figure 1: DTA data showing the range of annealing temperatures that allow only the ferromagnetic phase to crystallize (primary crystallization).

To confirm the crystallization of α'-FeCo, synchrotron X-ray diffraction was used. By conventional X-ray diffraction, it is difficult to differentiate between the disordered α-FeCo (bcc) and the ordered α'-FeCo (CsCl structure). The X-ray atomic scattering factors for Fe and Co are almost identical. Thus, the only difference between the α-FeCo and α'-FeCo diffraction patterns would be the faint superlattice reflections. The superlattice intensities are related to the square of the difference between the atomic scattering factors for Co and Fe, which remains very small. Therefore, using conventional X-ray diffraction would require long count times for the superlattice reflections to be resolved from the background radiation.

An alternative solution to the long count times necessary for conventional X-ray diffraction is to use synchrotron radiation. This has advantages due to the high intensity of the X-ray beam and the ability to choose a wavelength to take advantage of anomalous scattering. As seen in Figure 2, the (100) superlattice reflection verifies the α'-FeCo as the ferromagnetic phase.

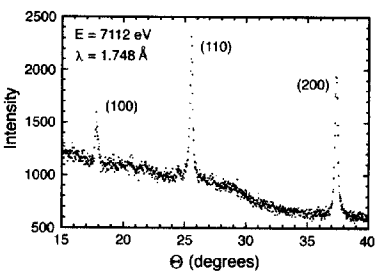

Figure 2: Synchrotron X-ray diffraction data showing the presence of α'-FeCo as the ferromagnetic phase from primary crystallization.

The formation of the desired ferromagnetic phase during primary solidification is critical for obtaining excellent soft magnetic properties since other phases might act as pinning sites for domain walls. Referring to Figure 1, the upper limit of the good annealing region is reached with the formation of undesired phases. Another important factor in the formation of the desired properties is proper nanocrystallization. According to the Herzer's theory, low coercivity is only

obtained for grain sizes well below (or well above) the exchange correlation length (~ domain wall width).[9-10] Thus, optimization of grain size is a necessity.

To obtain the optimum grain size in nanocrystalline alloys, an understanding of the crystallization kinetics is important. As a preliminary analysis of crystallization kinetics, the Kissinger technique has been used to find the activation energy for primary crystallization.[11-12] Figure 3(a) shows crystallization peaks at various heating rates. As the heating rate is increased, the primary crystallization peak shifts to higher temperatures due to a thermal activation necessary for crystallization. The Kissinger plot in Figure 3(b) shows this activation energy to be 323 kJ/mol (3.35 eV/atom). These values are similar to those for Fe-based nanocrystalline soft magnetic alloys.[14-15] By controlling the composition, number and distribution of nucleation sites, and quench rate of the amorphous precursor, we will be able to control the kinetics in similar materials and ultimately optimize the extrinsic magnetic properties.

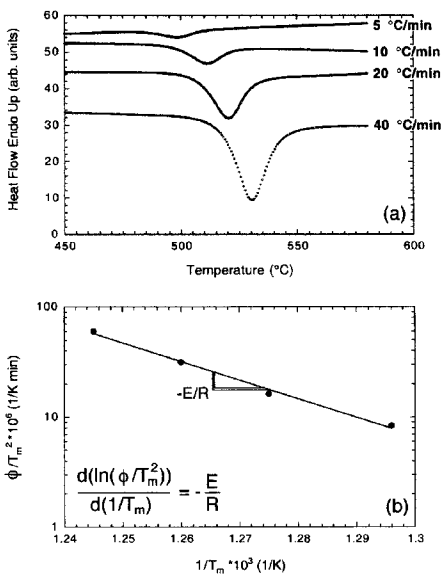

Figure 3: (a) DSC data showing the primary crystallization peak shift due to changes in heating rate (b) Kissinger plot used to determine the activation energy of primary crystallization

The stability of the nanocrystalline grains at high temperatures is essential for maintaining optimal magnetic properties. The chemical stability of the phases and minimization of grain growth of these alloys are both parameters which must controlled for use in high temperature applications. Both of these are concerns established by the Herzer and no pinning criteria already discussed.

To examine the stability of HITPERM, amorphous samples were annealed at 600 °C for up to 3072 hours. Each sample was examined by X-ray diffraction and the breadth of crystalline peaks were measured. The X-ray diffraction results shown in Figure 4, for the sample annealed for 3072 hours, showed that only the fundamental diffraction peaks for the α-FeCo were observed and that no secondary phase crystallization has occurred! This indicates that the stability of the nanocrystalline phase is maintained at high temperatures for long times and therefore these materials may be successfully used for high temperature applications.

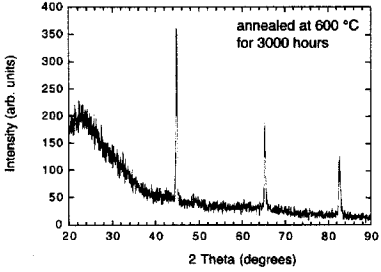

Figure 4: Conventional X ray diffraction showing nanocrystalline α-FeCo after annealing at 600 °C for 3072 hours

Nanocrystalline alloys, because of their small grain size exhibit significant fine particle broadening in the Bragg diffraction peaks. An empirical treatment of the fine particle broadening reveals that the particle size, t, can be determined from the breadth, B, of the x-ray peak as given by:

$$t = \frac{0.9\lambda}{B\cos\theta_B} \qquad [1]$$

that is known as the Scherrer formula.[13] It states that for a crystal of thickness, t, we should expect a particle broadening of B of the Bragg peak at $2\theta_B$. For 50 nm particles a broadening of ~0.20° is expected and is easily measured. Scherrer analysis has been used as a rough estimate of grain size for our annealed samples.

The Scherrer analysis results are summarized in Table II. The mean grain size seems to remain small over the whole range of annealing temperatures. Further support by transmission electron microscopy will be necessary to verify these preliminary results.

Annealing Time (hours)	D_{mean} (nm)	σ (nm)
10	49.39	17.12
31	36.52	10.33
100	70.89	12.97
308	57.97	32.96
1000	57.13	8.92
3072	61.18	14.03

Table II: Grain size by Scherrer analysis

In the similar FINEMET and NANOPERM alloys, a two phase microstructure has been observed as a ferromagnetic nanocrystalline phase and a ferromagnetic amorphous phase at the grain boundaries. The two-phase microstructure has been shown to aid the soft magnetic properties by: (a.) increasing the resistivity of the alloy thus reducing eddy current formation in

AC applications; (b.) decreasing the effects of magnetostriction since the amorphous and crystalline phases have magnetostrictive coefficients which effectively cancel out due to their sign differences, thus increasing the permeability. For these reasons, we would like to determine whether HITPERM has a similar two-phase microstructure.

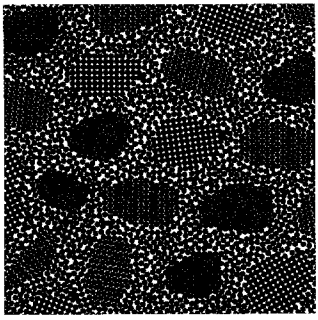

Figure 6: Schematic of a nanocrystalline alloy with amorphous grain boundary phase

Extended X-ray absorption fine structure (EXAFS) was used to examine the microstructure of the HITPERM alloy. As found in other nanocrystalline soft magnetic materials produced by the annealing of ribbons, the nanocrystalline phase is surrounded by a thin amorphous phase (see the schematic Figure 6). Since EXAFS is a technique that examines short range order, the very small amorphous phase region between nanocrystalline grains can be probed. Additionally, this technique is element sensitive allowing one to determine information as to the short-range order of the atoms whose absorption edge lies near the K edge of the element of interest. EXAFS studies described below have been used to determine the local environments of atoms in the nanocrystalline and amorphous intergranular phases. In particular, this study shows EXAFS data for ribbons annealed at 550, 650, and 800 °C at the Fe, Co, and Zr K edges.

Figures 7(a) and 8(a) show the Fourier transform (FT) Fe and Co EXAFS respectively. The data were collected from the as-spun sample and those annealed at 550, 650, and 800 °C. For comparison to a foil with a bcc structure, data from an Fe foil were also plotted. The ribbons are plotted using the left axis and the standard foil was plotted using the right axis.

The as-spun spectrum displays a well-defined near-neighbor (NN) peak with no signs of higher shell ordering. This is consistent with an amorphous structure. The sample annealed at 550 °C shows an increase in amplitude of the NN shell and a shift to higher radial distances. Additionally, higher order shells begin to appear. The peaks can be correlated directly to the bcc standard foil, but there is not enough r-space resolution to isolate each bond (i.e. $r_{1,2}$ and $r_{1,5}$). Comparison of the Fe or Co FT EXAFS with the Fe foil FT EXAFS shows a consistent bcc structure for our sample.

By plotting the NN peak amplitude and NN centroid as a function of the annealing temperature, insight into the structural evolution can be obtained. These results are plotted in Figures 7(b & c) and 8(b & c) respectively for Fe and Co. Both sets of data behave in a similar manner. As the annealing temperature increases, there is an abrupt increase in the NN average distance followed by a plateau (Figures 7(c) & 8(c)). This shows the transition of the NN peak from a single disordered atomic shell to that of a more ordered bimodal distribution of atoms. Increases in annealing temperature do not change this distance which is consistent with Fe and Co remaining in a bcc coordination.

The plots of the NN amplitude versus annealing temperature reveal a different trend. The amplitude increases without a plateau that indicates an increase in coordination and atomic ordering

(Figures 7(b) & 8(b)). This continuing increase in ordering and coordination indicates that even at annealing temperatures of 800 °C these features have not reached their equilibrium values.

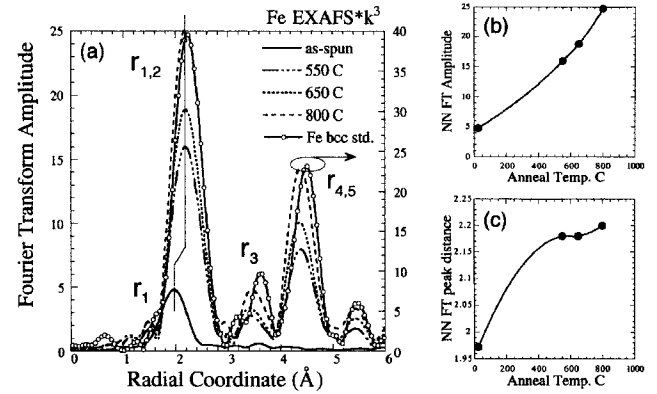

Figure 7: Fourier transform amplitude of Fe EXAFS showing BCC coordination of Fe

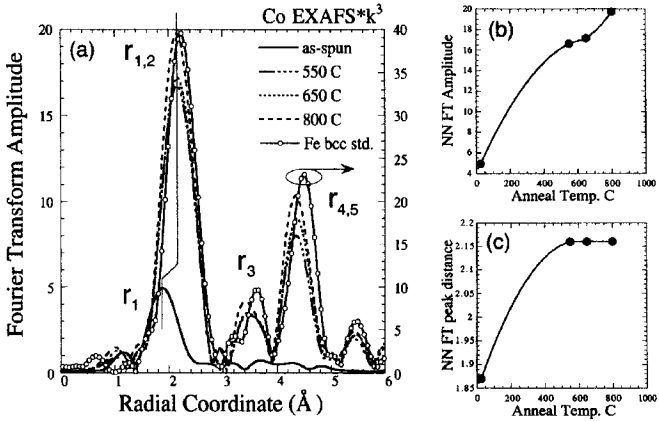

Figure 8: Fourier transform amplitude of Co EXAFS showing BCC coordination of Fe

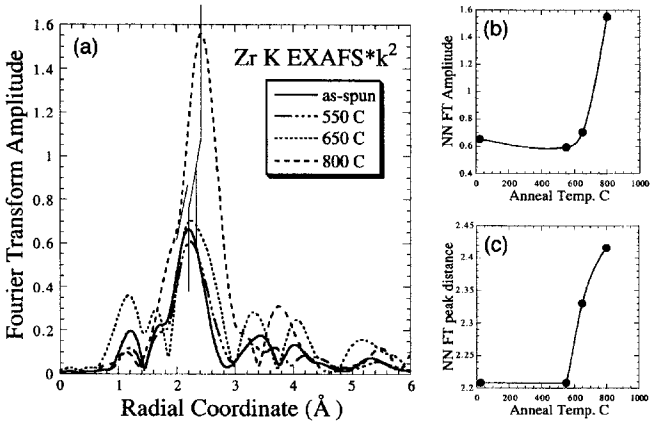

Figure 9: Fourier transform amplitude of Zr EXAFS showing coordination of Zr

The evolution of the local atomic environment of the Zr atoms is quite different from that of the Fe and Co atoms. The as-spun spectrum displays a well defined NN peak with two broad peaks having lower amplitude and at higher radial coordinates (Figure 9(a)). Although these peaks with higher radial distances may have structural origins, the atomic environment of Zr is clearly disordered and may be described as amorphous. After annealing at 550 °C, the NN coordination and distances have not changed much from the as-spun material. It is not until the sample is annealed at 650 °C that the peak distance begins to shift, but the amplitude still does not change much (Figure 9(b & c)). The sustained amplitude of the NN peak is evidence that the local environment of the Zr atoms remains amorphous. The change in the NN amplitude indicates that the local chemical order of the Zr atom is changing due to the formation of the FeCo crystallites. At 800 °C the amplitude of the NN peaks increases significantly and the distances continue to increase to higher radial values. This is a clear indication that the Zr atoms are significantly changing symmetry to a more ordered state (i.e. $(Fe,Co)_3Zr$).

B. Magnetic Properties

Curie temperature and magnetization are important intrinsic properties for high temperature applications. An amorphous precursor ribbon has been heated to observe the magnetization at high temperatures (Figure 10). Admittedly, the magnetization shown in Figure 10 is not the actual magnetization of the HITPERM alloy as it would be used. The magnetization in the nanocrystallized ribbon would be much higher since the effective annealing of the ribbon during this experiment is very short. However, this experiment shows some of the interesting phase transformations that occur in the HITPERM alloy.

As indicated in Figures 1, 10, and 11, heating of the amorphous ribbon with HITPERM composition shows primary and secondary crystallization, magnetic transformations, an order/disorder transformation, and a polymorphic phase transformation at the effective Curie temperature of the alloy.

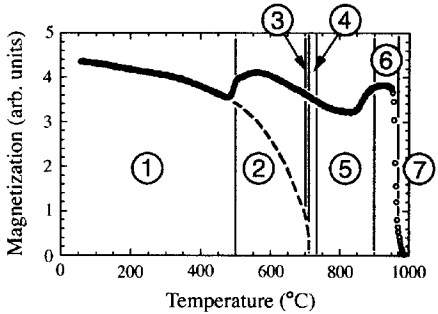

Figure 10: Thermomagnetic data taken from an amorphous sample with HITPERM composition.

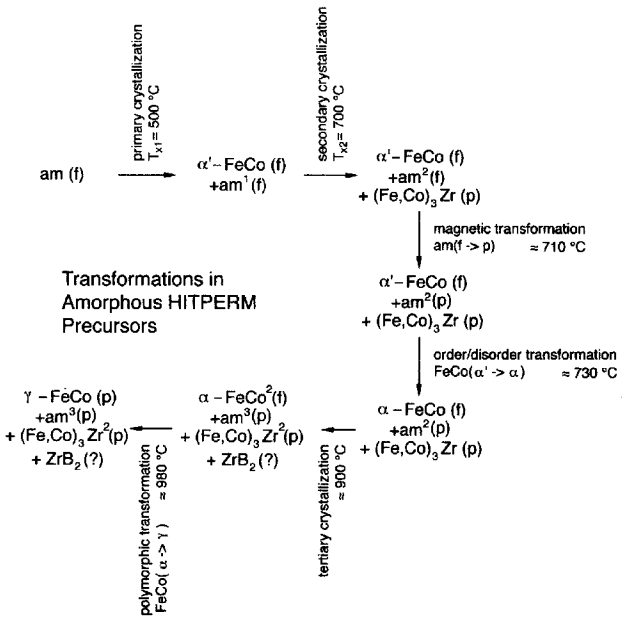

Figure 11: Phase transformations in HITPERM

The temperatures in Figure 11 are approximate for many of the transformations, and not all transformations are certain, but qualitatively the diagram shows many interesting aspects of the alloy. First of all, it is critical that the Curie temperature of the amorphous phase remain above the operation temperature of the alloy to avoid destroying the exchange coupling between grains and forming superparamagnetic particles of the nanocrystalline grains (or at least increasing the coercivity extensively). In all of the Fe-based nanocrystalline alloys, this is violated if the operating temperature is chosen as 500 °C. Therefore, operation of HITPERM should be limited to regions (1) and (2) of Figure 10, where the amorphous phase is ferromagnetic and no other crystalline phases have formed.

Another interesting aspect is the increase of the magnetization at high temperatures. This has been attributed to the formation of ZrB_2 or ZrO phases, yielding more α-FeCo. At 800 °C, the formation of α-FeCo is the only phase that will increase the magnetization, so formation of this ferromagnetic phase at the expense of paramagnetic $(Fe,Co)_3Zr$ seems likely.

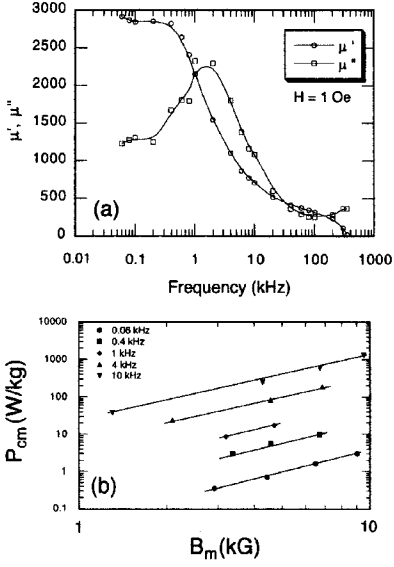

Figure 12: (a) Frequency dependent permeability for a field amplitude of 1 Oe (b) the core loss as a function of the maximum induction at various frequencies.

The extrinsic properties of interest include permeability and ultimately core loss in these alloys. In Figure 12(a), the frequency dependent permeability has been plotted for a field amplitude (H_m) of 1 Oe. The maximum permeability was determined to be 2900 and the peak in the loss portion of the permeability occurred at 2 kHz. However, an acceptable permeability of

1000 was maintained to 10 kHz. Figure 12(b) shows the core loss as a function of the maximum induction at various frequencies. Although the core loss seems quite high when compared to most Fe-based alloys, it is quite comparable to other FeCo-based alloys, which are used for high temperature applications

CONCLUSIONS

This work shows the formation of α'-FeCo phase as the ferromagnetic phase in a ribbon with a two phase microstructure. After annealing of nanocrystalline ribbons for up to 3000 hours at 600 °C, the ribbons show only small grain growth and no formation of secondary phases. Kinetics studies have shown an activation energy of 323 kJ/mol. Magnetization of the amorphous precursor ribbons show a high magnetization maintained to 980 °C. Permeability and core loss data show that HITPERM achieves the necessary magnetic properties for the intended application.

ACKNOWLEDGMENTS

Effort sponsored by the Air Force Office of Scientific Research, Air Force Materiel Command, USAF, under grant number F49620-96-1-0454. The U.S. Government is authorized to reproduce and distribute reprints for governmental purposes notwithstanding any copyright notation thereon. Work carried out in part at the National Synchrotron Light Source, Brookhaven National Laboratory, which is supported by the U.S. DOE, Divisions of Materials Sciences and of Chemical Sciences. Special thanks to Johnny Kirkland and Joseph Woicik for their help on Beamlines X23B and X23A2. Work carried out in part at Los Alamos National Laboratory, which is supported by the U.S. Department of Energy. DEL acknowledges partial support from NEDO project.

REFERENCES

1. Y. Yoshizawa, S. Oguma, and K. Yamauchi, *J. Appl. Phys.* **64**, 6044 (1988).
2. K. Suzuki, A. Makino, N. Kataoka, A. Inoue, and T. Masumoto, *Mat. Trans.* **JIM-32**, 93 (1991).
3. A. Makino, T. Hatanai, Y. Naitoh, T. Bitoh, A. Inoue, and T. Masumoto, *IEEE Trans. Magn.* **33**, 3793 (1997).
4. M. E. McHenry, M. A. Willard, and D. E. Laughlin. *Progress in Materials Science* (1999), in press.
5. M. A. Willard, D. E. Laughlin, M. E. McHenry, D. Thoma, K. Sickafus, J. O. Cross and V. G. Harris. *J. Appl. Phys.* **84**, 6773 (1998).
6. M. A. Willard, M.-Q. Huang, D. E. Laughlin, and M. E. McHenry, C. Franchetti, J. O. Cross, and V. G. Harris. *J. Appl. Phys.* **85** (1999) 4421.
7. H. Iwanabe, B. Lu, M. E. McHenry, and D. E. Laughlin. *J. Appl. Phys.* **85**, 4424 (1999).
8. J. D. Ayers, V. G. Harris, J. C. Sprague, and W. T. Elam, *Appl. Phys. Lett.* **64**, 974 (1994).
9. G. Herzer, *IEEE Trans. Magn.* **26**, 1397 (1990).
10. G. Herzer, *J. Magn. Mag. Mat.* **112**, 258 (1992).
11. H. E. Kissinger. *J. Res. Nat. Bur. Stand.* **57**, 217 (1956).
12. H. E. Kissinger. *Ana. Chem.* **29**, 1702 (1957).
13. B. D. Cullity, *Elements of X-ray Diffraction*, 2nd ed. (Addison-Wesley Publishing Company, Inc., Reading, MA, 1978), p. 102.
14. L. K. Varga. *Mat. Sci. and Eng.* **A179/A180**, 567 (1994).
15. C. F. Conde and A. Conde. *Mat. Lett.* **21**, 409 (1994).
16. K. Hono, A. Inoue, and T. Sakurai. *Appl. Phys. Lett.* **58** (1991) 2180
17. K. Hono, J. –L. Li, Y. Ueki, A. Inoue, and T. Sakurai. *Appl. Surf. Sci.* **67** (1993) 398
18. S. H. Kim, M Matsuura, N. Sakurai, and K. Suzuki. *Jpn. J. Appl. Phys.* **32** (1993) Supp. 32-2, 676
19. J. D. Ayers, V. G. Harris, J. C. Sprague, W. T. Elam, and H. N. Jones, *Acta Mater.* **46**, 1861 (1998).